ELSEVIER

Available online at www.sciencedirect.com

SCIENCE DIRECT®

International Journal of Solids and Structures 43 (2006) 4595–4615

INTERNATIONAL JOURNAL OF SOLIDS and STRUCTURES

www.elsevier.com/locate/ijsolstr

Identification of damage mechanism and validation of a fracture model based on mesoscale approach in spalling of titanium alloy

X. Boidin *, P. Chevrier, J.R. Klepaczko, H. Sabar

Laboratory of Physics and Mechanics of Materials, Ile du Saulcy, 57045 Metz Cedex 01, France

Received 16 March 2005; received in revised form 10 June 2005
Available online 10 August 2005

Abstract

The subject of this paper is identification of the physical mechanisms of spalling at low impact velocities for Ti–6Al–4V alloy and determination of the macroscopic stress of spalling via meso-macro approach. Spalling is a specific mode of fracture which depends on the loading history. The aspects of the initial microstructure and its evolution during plastic deformation are very important. In order to identify the spalling physical mechanisms in titanium alloy, numerous pictures by the optical microscopy of the spall surfaces created by plate impact technique have been taken. The scenario of failure observed is in complete agreement with known physical micro-mechanisms: namely nucleation, propagation and coalescence by adiabatic shearing of micro-voids. The most interesting point in spall fracture of Ti–6Al–4V alloy is the nucleation of micro-voids. A significant amount of small micro-voids in the region of the expected spall plane has been observed. It appears that microstructural effects are important due to dual α–β phase microstructure, called Widmanstätten structure. The orientation of microstructure has a direct influence on nucleation mechanism by means of distribution of nucleation sites and decohesion between the softer particles (α-phase lamellae) and the harder lattice (β-phase). According to these observations, a fracture model has been developed. This model is based on the numerous post-mortem microscopic observations of spall specimens. The goal is to determine the macroscopic stress of spalling in function of loading time and damage level via a meso-macro approach.

Keywords: Dynamic fracture; Spalling; Titanium alloy; Microstructure

* Corresponding author. Tel.: +33 3 87 31 53 56; fax: +33 3 87 31 53 66.
E-mail address: boidin@lpmm.univ-metz.fr (X. Boidin).

0020-7683/$ - see front matter © 2005 Elsevier Ltd. All rights reserved.
doi:10.1016/j.ijsolstr.2005.06.039

1. Introduction

The spalling is a dynamic phenomenon which occurs when two plane waves, an incident and a reflected one are superimposed leading failure by tension. It manifests itself by creation of a free surface inside the material. A setup for plate impact experiment has been developed in the Laboratory of Physics and Mechanics of Materials (LPMM) of Metz University to study dynamic fracture by spalling at impact velocity up to $V_{\text{impact}} \approx 600$ m/s (strain rates up to $\sim 10^6\ \text{s}^{-1}$). The lowest impact velocity in plate impact experiments was searched in function of the pulse duration in order to determine when the incipient spall occurs. Application of the acoustic approximation allowed to determine the critical normal stress for different pulse durations. Since only the minimum stress of spalling is searched for, the acoustic approximation yields a correct value of the critical failure stress. Because spalling is a specific kind of fracture which is loading history dependent, the effects of the initial microstructure and its evolution during local plastic deformation in the spall area are very important. It appears that microstructural effects are important in the case of titanium alloy Ti–6Al–4V due to dual phase microstructure. The first purpose of this study was to examine physical mechanisms of spall fracture for Ti–6Al–4V alloy on the incipient level and to identify the main stages of spalling in the meso-scale.

Series of tests at different impact velocities (from 290 m/s to 460 m/s) have been performed, and the level of the normal stress σ_{F} for the incipient spall in a function of the incident pulse duration t_{c} has been determined. Such analysis has yielded the preliminary data in the form of the critical tensile stress vs. the pulse duration, $\sigma_{\text{F}}(t_{\text{c}})$. In order to understand better the physical mechanisms of spalling, numerous scanning electron microscopy (SEM) pictures of the specimen surfaces after fracture have been taken for Ti–6Al–4V alloy. Some further observations and conclusions concerning the influence of microstructure on spall kinetics are presented in this paper.

Phenomenological or physical approaches, including micro-statistical one, can be applied to formulate fracture criteria for spalling, but still no universal one can be accepted. The approach by continuum damage mechanics, for example Cagnoux (1985), is based on introduction into the constitutive equations of one or more scalar or tensorial field quantities as measures of the material degradation. The micro-statistical approach is based on the microstructural description of damage by the continuum constitutive relations frequently formulated by notion of internal state variables. This approach is to some extent supported by experiments, Curran and Seaman (1987); Grady (1988). Because shorter times of loading produce higher values of the spall stress, which is typical feature for the spall phenomenon, Tuler and Butcher (1968) proposed a criterion based on the concept of cumulative process of failure. It was proposed by Dremin and Molodets (1985) that temperature and time dependence of the spall stress may be interpreted in terms of a modified Zhurkov's kinetic theory of fracture (Zhurkov, 1965). The early kinetic models of spalling based on thermal activation have also been discussed by Curran and Seaman (1987). In general, the cumulative criteria of spalling provide relatively good results in the macro-scale and they are quite useful in numerical codes (Hanim and Klepaczko, 1999).

It appears that, in the case of hard steels and hard titanium alloys, spalling involves as the first stage the mechanism of micro-crack nucleation and propagation and then coalescence of those micro-cracks by adiabatic shearing (Chevrier and Klepaczko, 1999). In order to gain a deeper insight on the material behavior during spalling, the initial microstructure of Ti–6Al–4V alloy has been examined by the optical microscopy and also by SEM observations, including chemical treatment of the surfaces.

2. Description of material

2.1. Material

The material studied was titanium alloy Ti–6Al–4V, with composition (in weight percent) given in Table 1. The industrial importance of titanium alloys is well known. They provide significant strength at low temperatures, good formability and weldability, and a range of attractive physico-chemical properties such as good corrosion resistance and good metallurgical stability. These properties make titanium alloys attractive candidate materials for many industrial applications. Ti–6Al–4V is currently used in a wide range of fields such as blades and discs for aircraft turbines, or surgical implants and dental prosthesis in medical domains.

Typical forming process of Ti–6Al–4V plates is as follows: (a) heated and rolled above the transus β (temperature above which the alloy is 100% β), (b) annealed twice, (c) rolled again and (d) controlled cooling. It is well known that titanium and its alloys are very sensitive to the final microstructure according to the way they are made. The production technology may introduce substantial changes in mechanical behavior. Thus, the microstructure of titanium alloys is affected by many technological factors, like thermal treatment and cooling rate after rolling.

2.2. Microstructure

In order to characterize the initial microstructure, some of the disk specimens were examined by optical microscopy. After polishing, the surfaces were chemically treated and then observed by an optical microscope. The following stages were applied:

- mechanical polishing with ground paper SiC with grains 2400 avoiding excessive normal force to avoid twinning,
- polishing with diamond paste on nylon fabric with grains 9, 6 and 3 μm up to shiny surface,
- chemical polishing with solution OP-S of Struers containing 30% of oxygen water,
- chemical treatment of surface with two following solutions:
  - composition 1
    HF: 4 ml, HNO_3: 8 ml, H_2O: 500 ml
  - composition 2
    HF: 2 ml, HNO_3: 4 ml, H_2O: 94 ml

Both solutions yielded good results for Ti–6Al–4V alloy with different time of submersion: in the case of composition 1:3 min and for composition 2:30 and 40 s.

The microscopy observation was performed for two directions: the direction of rolling, L–T-plane, and the perpendicular direction, L–S-plane. The microstructure in the direction of rolling is shown in Fig. 1(a). The first conclusion is that the microstructure is composed of colonies of grains with different orientations.

Table 1
Chemical composition of Ti–6Al–4V alloy (wt.%)

Element	Ti	Al	V	O	Fe	C	Mo	Ni
Ti–6Al–4V	89.149	6.28	4.16	0.176	0.151	0.025	0.026	0.033

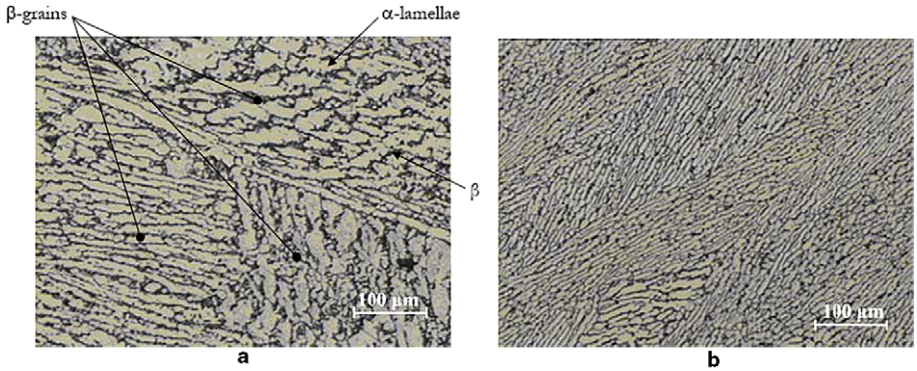

Fig. 1. Typical pictures of the Widmanstätten microstructure with α-phase lamellae (the white plates) separated by β-phase (dark regions) observed: (a) in the direction of rolling, L–T-plane, (b) in transverse direction, L–S-plane.

The microstructure in transverse direction is shown in Fig. 1(b). Once again, the microstructure is similar, but overall the grains are smaller. This is a typical Widmanstätten structure. The material consists of a duplex structure with a 70% volume fraction of α-phase lamellae embedded in β-phase (the remaining 30%) in a large β-grain as shown in Fig. 1(a). It may be mentioned that the phase α is a hexagonal close-packed (HCP) crystal structure and β is a body-centered cubic (BCC) one.

3. Experimental results

3.1. Experimental setup

Spalling of the Ti–6Al–4V alloy was studied by using plate impact experimental technique. Scheme of the arrangement in the form of the target plate and the flyer is shown in Fig. 2. Thin flyer plates of different thickness L_i and diameter 57 mm are launched with pre-programmed velocity (between 50 m/s to approx. 600 m/s) by the gas gun. The flyer plate strikes a flat stationary target plate of different thickness L_c. The

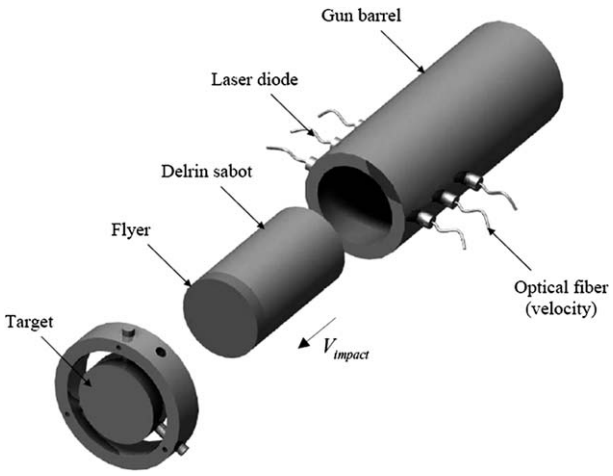

Fig. 2. Scheme of plate impact arrangement: target plate and flyer.

flyer plate and the target plate were made of the same material and they had the same diameter. The ratio of L_c/L_i was kept constant and equal 2.

The LPMM gas gun has four main parts: the pressure chamber of maximum pressure 250 bars with pneumatic breech, the barrel of length 2.88 m, the target chamber with optical window and electrical connections, as well as the catcher tank with a setup for soft recovery of plates. The pressure source may be nitrogen, helium or air. All plate impact experiments were performed in vacuum. The gas launcher is equipped with an electro-optical system to measure the impact velocity of the projectile also see Fig. 2 (Chevrier and Klepaczko, 1997). The launch pressure, the level of vacuum and all sequences of the launching are controlled by computer software. The system allows a good reproducibility of the experiment and also a high safety level.

3.2. Spall stress vs. loading time

If the stress amplitude and duration of the reflected wave, calculated by acoustic approximation using Eqs. (1) and (2), are high enough, spall occurs in the middle of the target when $L_c = 2L_i$.

The plate impact technique is very convenient in comparison to explosive loading because the velocity and planarity of impact can be precisely controlled in order to obtain an uniaxial state of deformation inside the target. In addition, an advancement of spalling can be stopped at different levels: incipient, intermediate and complete by using different flyer/target geometries and impact velocities. A direct application of the acoustic approach to estimate the critical conditions of spalling is justified for impact velocities slightly above the Hugoniot elastic limit (HEL). The critical time t_c after which spall occurs can be determined using the acoustic approximation, Eq. (1), which is the time interval from the beginning of the tensile loading in the middle of the target to the complete spall. During that interval the stress amplitude is σ_F. For the same material of flyer and target, the formulas for critical time and applied stress are

$$t_c = \frac{2L_i}{C_1} \quad \text{with } C_1 = \left(\frac{\lambda + 2\mu}{\rho}\right)^{\frac{1}{2}} \tag{1}$$

and

$$\sigma_F = \rho C_1 \frac{V_{impact}}{2}, \tag{2}$$

where λ, μ and ρ are respectively the elastic moduli (Lamé's and shear) and the density, L_i is the target thickness (varied) and V_{impact} is the impact velocity. Thus, with the input data L_i, V_{impact} and C_1, the two parameters σ_F and t_c are determined after each experiment. It means that for the given stress level σ_F the spall occurs at the time interval t_c. The targets were cut after each test along the plane parallel to the impact direction, L–S-plane. The surfaces were polished and examined under an optical microscope. Such procedure was applied to determine the state of material in the middle of target. The state is defined as

- no spall, which corresponds to the absence of micro-cavities or micro-cracks visible up to magnification ×1000,
- intermediate spall, which corresponds to the observation of numerous micro-voids or micro-cracks with a lower magnification than ×1000,
- complete spall, which corresponds to the formation of a macro-crack.

A series of 11 impact tests has been performed at room temperature on Ti–6Al–4V alloy within relatively wide range of impact velocities, from 290 m/s to 460 m/s. The final results in the form (σ_F, t_c) obtained for this alloy are presented in the Fig. 3. Table 2 shows experimental results in the form of the loading time t_c and critical stress σ_F.

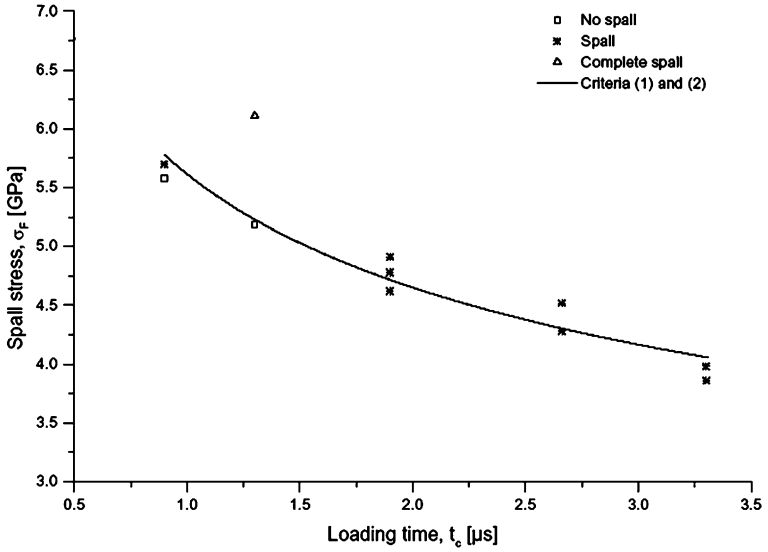

Fig. 3. Spall stress σ_F vs. loading time t_c for Ti–6Al–4V.

Table 2
Results of plate impact experiments

Target	L_i [mm]	V_{impact} [m/s]	t_c [μs]	σ_{appl} [MPa]	Level
1	3	420	0.9	5.58	No spall
2	3	429	0.9	5.70	Spall
3	4	460	1.3	6.11	Complete spall
4	4	391	1.3	5.19	No spall
5	6	370	1.9	4.91	Spall
6	6	360	1.9	4.78	Spall
7	6	348	1.9	4.62	Spall
8	8	340	2.66	4.52	Spall
9	8	322	2.66	4.28	Spall
10	10	300	3.3	3.98	Spall
11	10	291	3.3	3.86	Spall

3.3. Identification of parameters in the cumulative criterion of spall

It is known that spall fracture depends on numerous factors like loading time, local stress tensor, initial temperature and microstructure. Several formulas exist to predict spall fracture (Chevrier and Klepaczko, 1997). Those formulations represent three different approaches, namely physical, micro-statistical and phenomenological.

Klepaczko (1990) proposed an approach based on the Boltzmann statistics and formulated a cumulative fracture criterion for short and very short loading times or relatively low homologous temperatures. The critical time to fracture with the threshold stress σ_{F_0} is given by

$$t_{c_0} = \int_0^{t_c} \left(\frac{\sigma_F(t)}{\sigma_{F_0}} \right)^{\alpha(T)} dt, \qquad t_c \leqslant t_{c_0}, \quad \text{and} \quad \sigma_F \geqslant \sigma_{F_0}, \tag{3}$$

with

$$\alpha(T) = \frac{\Delta G_0}{kT}, \tag{4}$$

where σ_{F_0}, t_{c_0} and α are three material constants at constant temperature T. t_{c_0} is the longest critical time when $\sigma_F(t_{c_0}) = \sigma_{F_0}$, for $t_c > t_{c_0}, \sigma_F = \sigma_{F_0}$. In general, the exponent $\alpha(T)$ is temperature dependent and is related to the activation energy of material separation ΔG_0. When the process is nonisothermal, the exponent $\alpha(T)$ is temperature and time-dependent, $\alpha(T,t) = \Delta G_0/kT(t)$, and Eq. (3) must be integrated accordingly. Several forms of the $\sigma_F(t)$ histories were analyzed by Klepaczko (1990). For the case of square pulse $\sigma_F(t) = \sigma_F H(t)$, where $H(t)$ is the Heaviside step function and with the constant temperature, the criterion takes the form

$$\sigma_F(t_c) = \sigma_{F_0}\left(\frac{t_{c_0}}{t_c}\right)^{\frac{1}{\alpha}}, \tag{5}$$

and

$$t_c(\sigma_F) = t_{c_0}\left(\frac{\sigma_{F_0}}{\sigma_F}\right)^{\alpha}. \tag{6}$$

In order to take into account the effect of initial temperature on the spall stress σ_F, it was recently assumed that the threshold stress σ_{F_0} diminishes according to the thermal softening of the material lattice. Thus, the effect of temperature on the threshold stress is defined as

$$\sigma_{F_0}(T) = \frac{\mu(T)}{\mu_0}\sigma^{\circ}_{F_0}, \tag{7}$$

where $\mu(T)$ is the temperature-dependent shear modulus, and μ_0 and $\sigma^{\circ}_{F_0}$ are respectively the shear modulus and the threshold stress at zero of absolute temperature. A convenient expression for the relative changes of the elastic constants as a function of temperature is given by Klepaczko (1988) as

$$\frac{\mu(T)}{\mu_0} = 1 - \frac{T}{T_m}\exp\left[\theta^*\left(1 - \frac{T_m}{T}\right)\right], \tag{8}$$

where T_m is the melting point and θ^* is the homologous characteristic temperature. The modified threshold stress is in the following form:

$$\sigma_{F_0}(T) = \sigma^{\circ}_{F_0}\left\{1 - \frac{T}{T_m}\exp\left[\theta^*\left(1 - \frac{T_m}{T}\right)\right]\right\}, \tag{9}$$

and generalized cumulative criterion is given by

$$t_{c_0} = \int_0^{t_c}\left\{\sigma_F(t)\left[\sigma^{\circ}_{F_0}\left(1 - \frac{T}{T_m}\exp\left(\theta^*\left(1 - \frac{T_m}{T}\right)\right)\right)\right]^{-1}\right\}^{\alpha(T)}. \tag{10}$$

For the square incident wave $\sigma_F = \text{const}$, and with Eqs. (5), (10) is simplified to

$$\sigma_F(t_c, T) = \sigma^{\circ}_{F_0}\left\{1 - \frac{T}{T_m}\exp\left[\theta^*\left(1 - \frac{T_m}{T}\right)\right]\right\}\left(\frac{t_{c_0}}{t_c}\right)^{\frac{\Delta G_0}{kT}}, \tag{11}$$

with T as a parameter and for the square incident wave.

Criterias (1) and (2) are listed in Table 3. Assuming the acoustic approximation and rectangular shape of the incident wave, the material constants of the spall criteria have been determined at room temperature for

Table 3
Summary of proposed criteria

Criterion	Formulation	Constants
1 (Simplified)	$\sigma_{\mathrm{F}} = \sigma_{\mathrm{F}_0}\left(\frac{t_{\mathrm{c}_0}}{t_{\mathrm{c}}}\right)^{kT/\Delta G_0}$	$\sigma_{\mathrm{F}_0},\ t_{\mathrm{c}_0},\ \Delta G_0$
2 (Generalized)	$\sigma_{\mathrm{F}} = \sigma^0_{\mathrm{F}_0}\left[1 - \frac{T}{T_{\mathrm{m}}}\exp\left(\theta^*\left(1 - \frac{T_{\mathrm{m}}}{T}\right)\right)\right]\left(\frac{t_{\mathrm{c}_0}}{t_{\mathrm{c}}}\right)^{1/\alpha}$	$\sigma^0_{\mathrm{F}_0},\ T_{\mathrm{m}},\ \theta^*,\ t_{\mathrm{c}_0},\ \Delta G_0$

Table 4
Summary of criteria constants for Ti–6Al–4V alloy

Criterion	σ_{F_0} [GPa]	t_{c_0} [μs]	α	ΔG_0 [eV]	T_{m} [K]	θ^*
1	4.165	3	3.676	0.0928		
2	4.265	3	3.676	0.0928	1900	0.344

Ti–6Al–4V alloy. In numerical simulations, these criteria give very good results in prediction of the incipient spall and the free surface velocity profiles, for both elasto-plastic and elasto-viscoplastic cases (Hanim and Klepaczko, 1999). Because of an unique value of α, the values for the limiting point $(\sigma_{\mathrm{F}_0}, t_{\mathrm{c}_0})$ must be assumed. The quasi-static value of the threshold stress σ_{F_0} can be found by standard fracture mechanics methods. As a first approximation, value of t_{c_0} is assumed as 3.0 μs and σ_{F0} is assumed as value equal to the HEL. After analysis of experimental data, Fig. 3, the following set of values has been obtained in Table 4. Criteria (1) and (2) are plotted in Fig. 3 assuming room temperature.

Because value of α is directly related to the activation energy ΔG_0, it is possible to calculate the value of that energy with Boltzmann constant $k = 8.617 \times 10^{-5}$ eV/K, the result is: $\Delta G_0 = 0.0928$ eV. The activation energy in thermally activated processes of plastic deformation is usually estimated for pure Ti as $\Delta G_0^{\mathrm{pl}} = 0.68$ eV (Klepaczko, 1988). Thus, this value is much higher than the value found via spalling. The ratio of those energies is 0.14. It indicates the existence at the same time of plasticity and quasi-brittle mechanism of material separation. If the activation energy of spalling was close to zero the failure would be purely brittle.

It is interesting to note that analysis of experimental data for spalling of aluminum alloy 7020-T6 and armor steel Mars 190 yielded the following set of constants, Al alloy: $\sigma_{\mathrm{F}_0} = 1.068$ GPa and $\alpha = 1.360$, Mars 190: $\sigma_{\mathrm{F}_0} = 4.9$ GPa and $\alpha = 2.369$ (Chevrier and Klepaczko, 1999). The activation energies ΔG_0 for these two materials are ΔG_0 (7020-T6) $= 0.034$ eV and ΔG_0 (Mars 190) $= 0.059$ eV. Once again, the values of the mean activation energies for the process of spalling are the global values for all physical processes involved in the material separation. This is why the activation energy for spalling is always lower than for a "pure" (one-dimensional stress) plasticity. The lowest activation energies of spalling indicate a failure (free surface) with a small contribution of plasticity. This is observed for all almost brittle mechanisms of material separation. In conclusion, an assistance of thermal energy of atoms is omnipresent in all mechanisms of fracture and it must be taken into consideration in the time-dependent critical stress for spalling. This idea is not quite new, see for example Curran and Seaman (1987), but still is a source of new applications.

4. Metallographic observations of targets

Metallographic observations of the targets have been performed in order to determine the damage mechanisms in spalling of the Ti–6Al–4V alloy. The scenario of failure observed by SEM, which occurs during

spall fracture, is in complete agreement with known physical micro-mechanisms: namely nucleation of micro-voids, propagation and next coalescence of those micro-voids by adiabatic shearing.

Some further observations and conclusions concerning the influence of microstructure on spall kinetics are given below. In general, fracture in metals is a result of combination of two modes of material separation which are brittle and ductile. The contribution of each mode to the final separation changes with initial test temperature, time of loading, and of course, the initial microstructure. Brittle fracture dominates when a micro-crack is initiated on the meso-scale (0.1–10 μm) with contribution of a small plastic deformation. Ductile fracture dominates when it occurs simultaneously with the local plastic deformation larger than a certain threshold. Typical contribution of plasticity in the early stage of failure is the mechanism of micro-voids. At low temperatures and high loading rates including spalling, nucleation is governed by critical stress, and the micro-cracks or the micro-voids nucleate and grow from preexisting inhomogeneities like grain boundaries, boundaries of different phases and inclusions. An interesting point in the analysis of Ti–6Al–4V alloy is nucleation of the specific micro-voids. A significant amount of micro-voids in the region

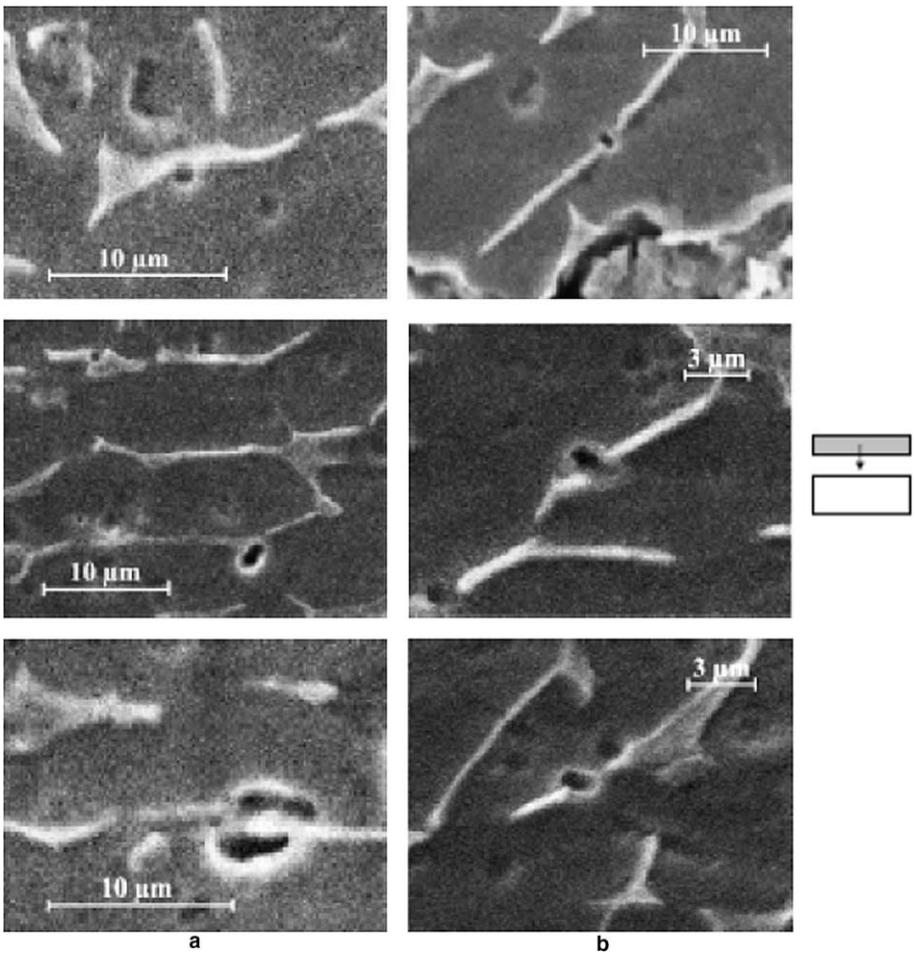

Fig. 4. Micro-voids in the initial stage of failure localized: (a) in the interface α/β, direction parallel to the wave front, (b) in junction of the α/β phase.

of the expected spall plane was observed. The micro-voids were preferentially located on the boundaries of α-grains and lamellar α–β boundaries. It was also observed that the voids were located on triple points.

The specimen of Ti–6Al–4V spalled in the following conditions: $V_{\text{impact}} = 290$ m/s, $t_c = 3.3$ μs, $\sigma_F = 3.68$ GPa, has been analyzed by SEM in details. It was found that the mechanism of failure is similar to what was reported by Arrieta and Espinosa (2001). However, two micro-mechanisms of the initial stage of failure are found. The first micro-mechanism is shown in Fig. 4(a). This is the case when lamellae are oriented in parallel to the plane of impact. The micro-voids occur at the interface of α–β phases, they are located to the boundaries of α-grains and lamellar α–β. The size of those initial micro-voids is relatively small $\sim$1.0 μm. The second micro-mechanism of the initial stage of failure is shown in Fig. 4(b). Some examples of this stage of failure found on SEM pictures are convincing. The lamellae are inclined to the impact plane. The micro-voids are localized between the junction of two β-phases.

A more advanced stage of such micro-damage is shown in Fig. 5(a) where a micro-void is grown and allows to imagine easily the linking mechanisms of the micro-voids when the lamellae are inclined. When the coalescence of micro-voids is complete, spallation takes a very particular aspect because it accommodates itself perpendicularly to the α and β-lamellae by linking the micro-voids. In Fig. 5(b), the perpendicular aspect of the spallation when the lamellae are inclined can clearly be seen. This fracture is formed by junction of the initial micro-voids.

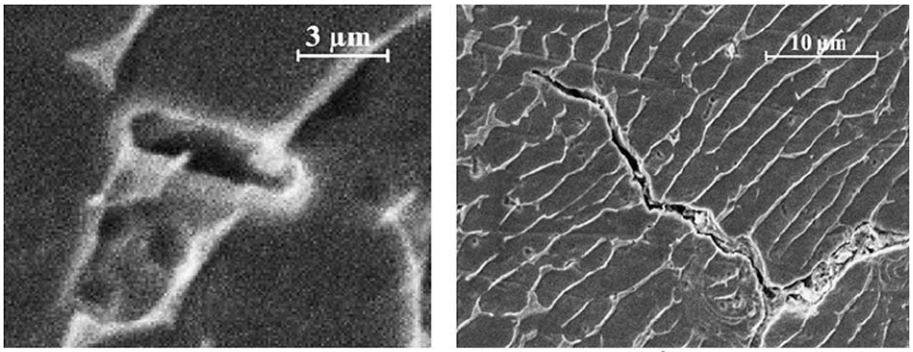

Fig. 5. Micro-crack in the stage of growth (a), perpendicular to the lamellae direction (b).

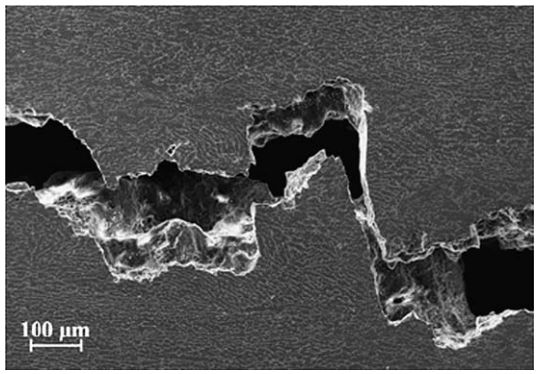

Fig. 6. Profile of fracture surface for Ti–6Al–4V alloy.

The observations confirm that the spall process is a result of nucleation, growth and coalescence of micro-cracks and micro-voids. Thus, during the latest stages, the spalling is controlled by the local plastic deformation via coalescence of micro-cracks and micro-voids and development of local adiabatic instabilities between them (internal adiabatic shearing or adiabatic micro-necking of adjacent micro-cavities). It is clear that the microstructure has a direct influence on the mechanism of nucleation, growth and coalescence of micro-cracks and micro-cavities by means of the distribution of nucleation sites. When the micro-cavities are large enough, a high-speed lateral expansion leading to adiabatic plastic shearing between theses occurs. The final stage of material separation is shown in Fig. 6. The relief shown in this picture is one of many possibilities and it depends perhaps on the initial hardness of an alloy. It may be also mentioned that other failure profiles are reported for Ti–6Al–4V in literature (Arrieta and Espinosa, 2001; Me-Bar et al., 1987). Another unknown factor, which is very important in the final micro-mechanism of separation, is the effect of impact velocity V_{impact}. Higher impact velocities may involve a more turbulent plastic deformation in the process zone of spalling (Mescheryakov et al., 1999).

5. Meso-model of spalling with thermal coupling

In general, the cumulative criteria of spalling, for example that discussed in the previous section provide good results in the macro-scale and they are quite useful in numerical codes, for example numerical study by Hanim and Klepaczko (1999). It appears that in case of Ti–6Al–4V alloy, the spall involves the mechanism of micro-crack nucleation and propagation and next coalescence of those micro-cracks by adiabatic shearing. Such approach to analyse spalling is based on meso-scale observations all along the entire cross-section of a target, which quantify the contribution of quasi-brittle and ductile fracture which may also include adiabatic shear banding. A fracture model proposed by Klepaczko and Chevrier (2003) has been developed. Its goal is to determine the macroscopic stress of spalling in function of loading time and damage level via a meso-macro approach.

In the following parts of the paper, results of the measurements which have been performed on the spalled target 5 with incipient advancement of spalling are discussed. The characteristics of this target are given in Table 2. The critical time $t_c = 1.9$ μs after which spall occurs and the spall stress $\sigma_F = 4.91$ GPa are obtained with a direct application of the acoustic approach.

5.1. Remarks on statistical distribution of dimples

This part reports results of microscopic measurements in the form of statistical distribution of horizontal meso-segments of fracture surface of targets, corresponding to expansion and coalescence of micro-cavities in horizontal direction (parallel to the plane wave), and vertical meso-segments, corresponding to ductile fracture and/or adiabatic shear banding (perpendicular to the plane wave). The vertical direction is the direction of the wave propagation, see Fig. 6. The procedure of measurement for Ti–6Al–4V alloy is applied all along the entire target cross-section of length 57 mm. For each cross-section of a fractured specimen, more than hundred measurements were taken. A typical spall section with characteristic dimensions is presented in Fig. 7, ΔX_i is the length of horizontal segment, parallel to the impact plane, which appears during the first step of quasi-brittle nucleation. The length of vertical segment perpendicular to the impact plane is denoted by ΔY_i. This occurs later during local plastic deformation and adiabatic shear banding. In order to construct a model for this meso-mechanism, it is important to know the distribution of ΔX_i and ΔY_i all along the entire cross-section of a target. Thus, the spalled cross-section was divided into 114 elements that had constant length of 500 μm. Microscopic observation of each element allows to measure all ΔX_i and ΔY_i lengths. Such meso-mechanism of spalling can be approximated by elementary cell composed of a horizontal segment of average length $\overline{\Delta X_i}$, a vertical segment of average length $\overline{\Delta Y_i}$ and with an adiabatic shear

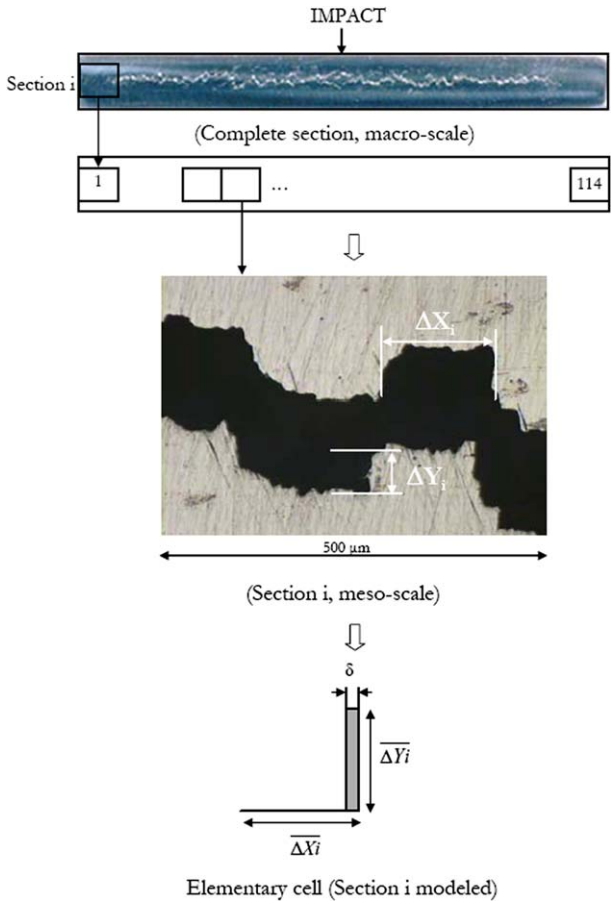

Fig. 7. Characteristic dimensions of spalled cross-section, Ti–6Al–4V alloy.

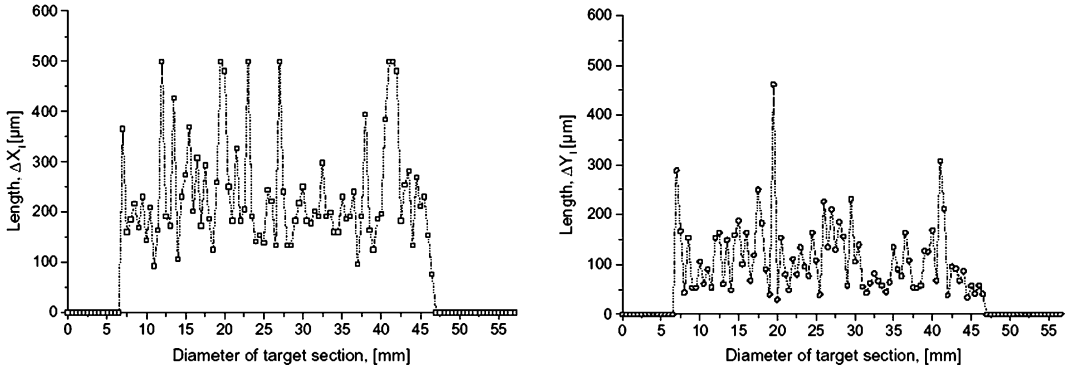

Fig. 8. Distribution of segment dimensions parallel (ΔX_i) and perpendicular (ΔY_i) to the impact plane along the cross-section, Ti–6Al–4V alloy, $V_{impact} = 370$ m/s, $t_c = 1.9$ µs, mean values $\overline{\Delta X_i} = 236$ µm, $\overline{\Delta Y_i} = 112$ µm.

band of average width δ, as it is shown in Fig. 7. The spatial distribution of characteristic dimensions on the target 5 is presented in Fig. 8.

It is clear that a sufficient amount of experimental evidence has now been gathered to confirm the scenario of spalling which involve a series of events in the micro and meso-scales. Such scenario can be applied directly to formulate a new model of spalling already analyzed for an armor steel by Klepaczko and Chevrier (2003); Boidin et al. (2003).

5.2. Modelling on meso-level

5.2.1. Nucleation and propagation of a crack

Since the microscopy observations indicate that the criterion for spalling based on the coalescence of micro-voids or micro-cracks and adiabatic shearing is applicable for titanium alloys, it is assumed that the new model based on the elementary cell can be also applied for Ti–6Al–4V. The first step for an elementary cell model, shown in Fig. 7, is the nucleation and propagation of micro-cracks. Although start of voids and cracks nucleation cannot be considered as simultaneous events, it is here assumed that the best approximation is to use the mean values of the nucleation time. This phenomenon starts when the local stress exceeds the particle-matrix critical stress σ_d of decohesion. In case of a preliminary approach, the concept of elastic brittle fracture proposed by Griffith, is generalized to metals by adding to the elastic surface energy, γ_e, a supplementary surface energy corresponding to plastic dissipation, γ_p. In such case, the critical stress σ_d is given by the relation

$$\sigma_d(t) = \sqrt{\frac{\xi E \gamma_R}{(1-\nu^2)\Delta X_i(t)}}$$

and

$$\Delta X_i(t) = f(V_f, a_{moy}, t), \tag{12}$$

where $\xi = \pi/2$ for a penny-shape and $\xi = 2/\pi$ for a plane crack, E is the Young's modulus ($E = 115$ GPa), ν is the Poisson's ratio ($\nu = 0.33$) and $\gamma_R = \gamma_e + \gamma_p$ is the surface fracture energy ($\gamma_e = 10^{-6}$ J/mm^2). According to Orowan (1948), the surface energy of plastic deformation in the case of metals is approximately three orders of magnitude higher than the elastic surface energy. It was assumed in the present analysis that the plastic surface energy is proportional to the elastic surface energy, $\gamma_p = \chi\gamma_e$, where χ is the coefficient of proportionality, it is usually assumed that $\chi = 10^3$. In the model, $\Delta X_i(t)$ is the length of micro-crack at time t for cell number i, V_f is the crack velocity and a_{moy} is the average length of heterogeneities.

Under the effective local stress σ_d, the micro-crack propagates at velocity V_f up to attainment its final length. According to Gilman's theory (1960), the propagation velocity increases with the size of the crack to become infinite at the edge of the material. In our case, the crack propagates locally and stops because of the local unloading. Therefore, it was chosen to assume a crack velocity which passes quickly by a phase of growth between $[t_d, t_a/2]$ and then remains constant between $[t_a/2, t_a]$, until the crack stops.

$$\begin{aligned} &\text{For} \quad t \leqslant \frac{t_a}{2}, \quad \Delta X_i(t) = \frac{2V_f}{t_a}t^2 + a_{moy} \\ &\text{For} \quad t \geqslant \frac{t_a}{2}, \quad \Delta X_i(t) = 2V_f t + a_{moy} - \frac{V_f t_a}{2} \end{aligned} \tag{13}$$

where t_d is the time when the micro-crack starts to propagate, t_a is the propagation time which is given by the relation

$$t_a = \frac{\overline{\Delta X_i} - a_{moy}}{\frac{3}{2}V_f} \tag{14}$$

5.2.2. Growth and coalescence by adiabatic shear band

This stage needs more energy than nucleation and propagation stages. Under tension load, the plastic deformation is localized within a small shear zone between two neighbouring micro-cracks situated on different levels. Evolution of the shear stress in this zone has a typical evolution history for adiabatic shear band as discussed by Marchand and Duffy (1988); Wright and Ockendon (1992). In this stage of the modelling, it is assumed that plastic deformation increases abruptly up to the critical value of shear deformation Γ_c, which is the instant when the shear failure starts to propagate. In other terms, the vertical segment ΔY_i is rupturing within the core of the micro-shear band of thickness δ. The progressive cracking of the adiabatic shear band is continued at constant velocity V_b until a complete coalescence of two neighbouring micro-cracks. The plastic deformation in the shear band is given by the relation

$$\Gamma_p = \frac{V_b t}{\delta}. \tag{15}$$

It is possible to distinguish three stages in development of the adiabatic shear band in the $\tau(\Gamma)$ coordinates, where τ is the shear stress and Γ is the shear gradient (Marchand and Duffy, 1988). The first stage is reached when the shear stress is at the maximum. The second corresponds to a slight decreasing of stress where deformation becomes inhomogeneous and the last one corresponds to a rapid stress decrease that signals a fast localization of deformation. The growth of micro-cavities occurs during the second stage of shearing and the coalescence of neighbouring micro-cracks occurs only during the stage three. In the model, in order to determine evolution of the shear stress inside the band, only the final stage is considered. The local evolution of the shear stress τ is calculated for a plastic material with the linear thermal softening proportional to the homologous temperature and the constant rate sensitivity m by using the following constitutive relation, (Wright and Ockendon, 1992).

$$\tau(\dot{\Gamma}_p, T) = \tau_0 \left(1 - a\frac{T}{T_m}\right)\left(1 + b\frac{\dot{\Gamma}_p}{\dot{\Gamma}_0}\right)^m, \tag{16}$$

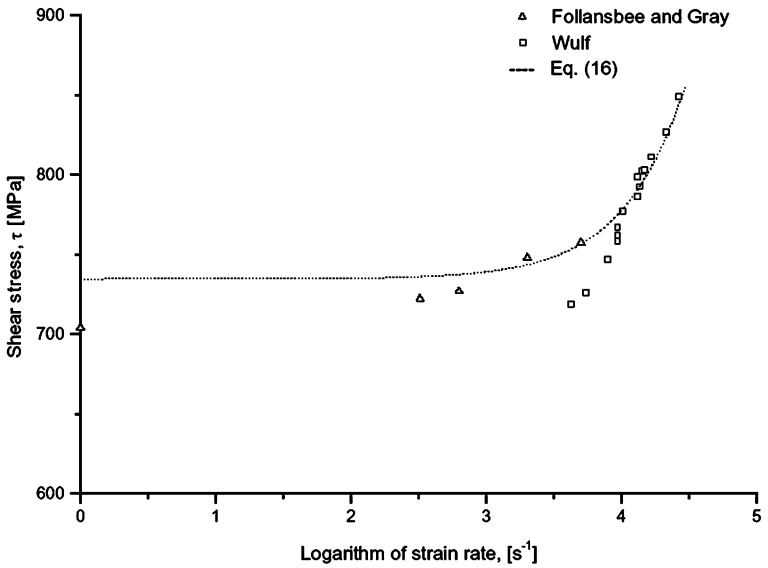

Fig. 9. Shear stress vs. log of strain rate $\tau(\log \dot{\Gamma}_p)$, T = 273 K, Follansbee and Gray (1989); Wulf (1979).

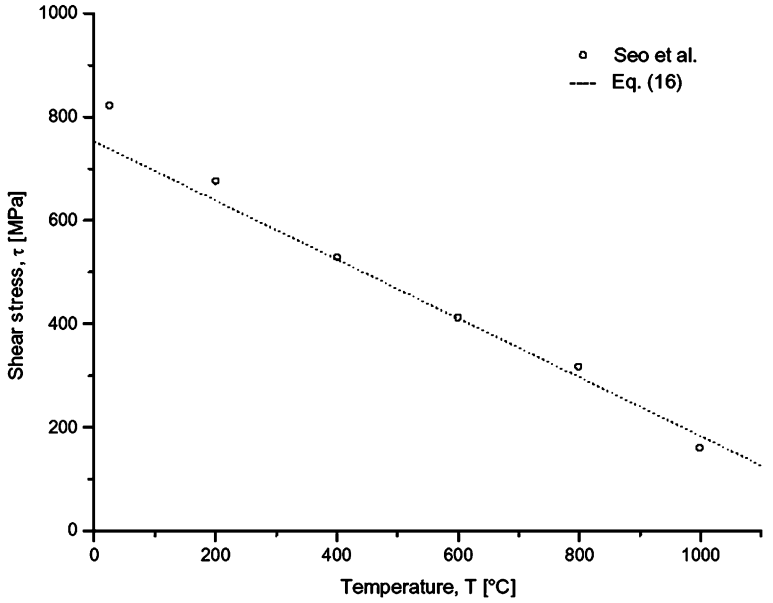

Fig. 10. Shear stress vs. temperature $\tau(T)$, $\dot{\Gamma}_p = 1400\ s^{-1}$, Seo et al. (2005).

Table 5
Material constants in the constitutive relation (16) for Ti–6Al–4V alloy

τ_0 [MPa]	a	T_m [K]	b	$\dot{\Gamma}_0$ [s^{-1}]	m
900	1.192	1900	0.122	10^4	0.494

where T_m is the absolute melting temperature ($T_m = 1900$ K), T is the current temperature, $\dot{\Gamma}$ (s^{-1}) is the strain rate, $\dot{\Gamma}_p$ (s^{-1}) is the shear strain rate of plastic deformation, $\dot{\Gamma}_0$ (s^{-1}) is the reference strain rate, a is the constant related to the temperature sensitivity, b is the constant related to the rate sensitivity, and τ_0 (MPa) is the threshold stress. Some constants, more exactly a, b and m, have been determined for Ti–6Al–4V by simple tension or compression tests at different strain rates, see Fig. 9 (Follansbee and Gray, 1989; Wulf, 1979), and temperatures, Fig. 10 (Seo et al., 2005). The constitutive relation, Eq. (16), is plotted in Figs. 9 and 10 in dotted line. Values of optimized material constants are listed in Table 5.

5.2.3. Equations for three phases of spalling

Finally, all these simplifications and derivation steps have allowed to define the model for the one elementary cell. The model permits to estimate the evolution of the mean normal stress in the macro scale as a function of time or damage evolution level in the meso-scale. All three stages of the modelling are depicted in Table 6, where in this table F^{meso} is the mesoscopic strength which is applied on the area of considered cell, S_{cell}. With the symmetry in the X and Y directions, the active area is equal to the square of $\overline{\Delta X_i}$, as it is shown in Fig. 11. The elementary surface is S_{pl} on which the shear stress is applied. For the same reasons of symmetry in the Y and Z directions, this area is a square of $\overline{\Delta Y_i}$ side.

In the last stage of the modelling, when the failure of adiabatic shear band starts, it is assumed that shear strain is constant in the cohesive zone and is equal to its value just before the beginning of failure: $\tau(t_{sh})$. The shearing velocity of the band separation is V_c.

Table 6
Three phases of failure in the meso-model of spalling

Nucleation and propagation of micro-crack	
$t_d \leqslant t \leqslant t_a$	$t_a = \frac{\overline{\Delta X_i} - a_{moy}}{\frac{3}{2}V_f}$
$\sigma^{meso} = \sigma_d$	$\sigma_d(t) = \sqrt{\frac{\xi E \gamma_e (1+\chi)}{(1-\nu^2)\Delta X(t)}}$
Nucleation and propagation of adiabatic shear band	
$t_a \leqslant t \leqslant t_a + t_{sh}$	$t_{sh} = \frac{\delta \Gamma_c}{V_b}$ (Eq. (15))
$\sigma^{meso} = \frac{F^{meso}}{S_{cell}}$	$S_{cell} = \overline{\Delta X_i}^2$
$F^{meso} = \tau(t) S_{pl}$	$S_{pl} = \overline{\Delta Y_i}^2$
$\tau(t)$ (Eq. (16))	
Failure of adiabatic shear band	
$t_a + t_{sh} \leqslant t \leqslant t_a + t_{max}$	$t_{max} = \frac{\delta \Gamma_c}{V_b} + \frac{\Delta Y_i}{2V_c}$
$\sigma^{meso} = \frac{F^{meso}}{S_{cell}}$	$S_{cell} = \overline{\Delta X_i}^2$
$F^{meso} = \tau(t_{sh}) S_{pl}$	$S_{pl} = [\overline{\Delta Y_i} - V_c(t - t_{sh})]^2$
$\tau(t_{sh})$ (Eq. (16))	

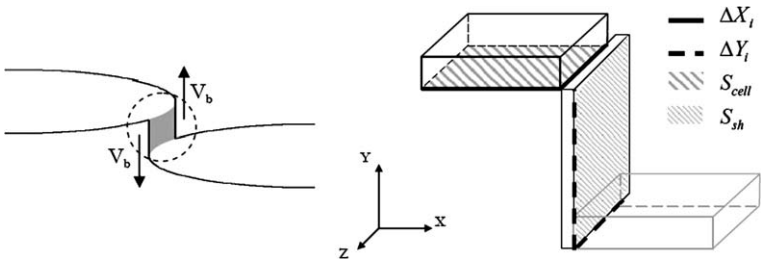

Fig. 11. Localization of plastic deformation within a small shear zone between two neighbouring micro-cracks situated on different levels.

5.3. Results and discussion

The model discussed here has been applied to the target 5. In order to determine the mean values, the spalled cross-section was divided into 114 sub-sections. In every sub-section, ΔX_i and ΔY_i were measured. Then, the average values of all ΔX_i and all ΔY_i were calculated. Next, an elementary cell corresponding to all cross-sections was found. Having the mean dimensions $\overline{\Delta X_i}$ and $\overline{\Delta Y_i}$ of the elementary cell, the local mean mesoscopic stress vs. time for one elementary cell could be obtained and the result is plotted in Fig. 12. All three stages of spalling are clearly recognizable.

When the mesoscopic normal stress in function of time is defined, the macro stress in function of time can be calculated. For that purpose, this operation was performed for all 114 sections. The mesoscopic normal stress of spalling was determined in function of time by finding the average of the mesoscopic stresses of all elementary cells. An application of EXCEL in Visual Basic programming language was created and the time evolution of the macro stress was found for the target 5, the result is shown in Fig. 13. Definition of the mesoscopic normal stress σ^{meso} parallel to the spall plane is given in Table 6.

All results have been obtained with the hypothesis that all elementary cells nucleate at the same time. Two things can noticed on the curves shown in Fig. 13. First of all, beyond $t = 1$ μs, the curve becomes discontinuous. Then, at the loading time $t_c = 1.9$ μs (Table 2), during which the target is under load, is sub-

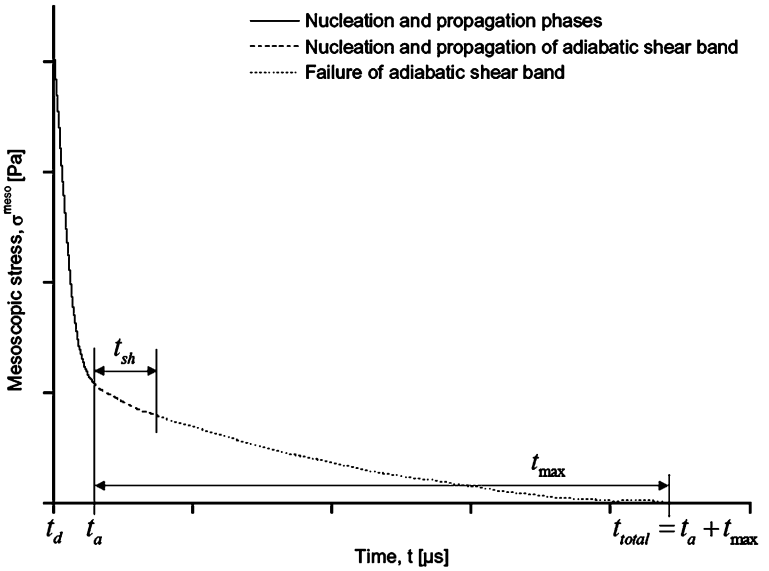

Fig. 12. Schematic evolution of the mesoscopic normal stress vs. time $\sigma^{\text{meso}}(t)$ for one elementary cell.

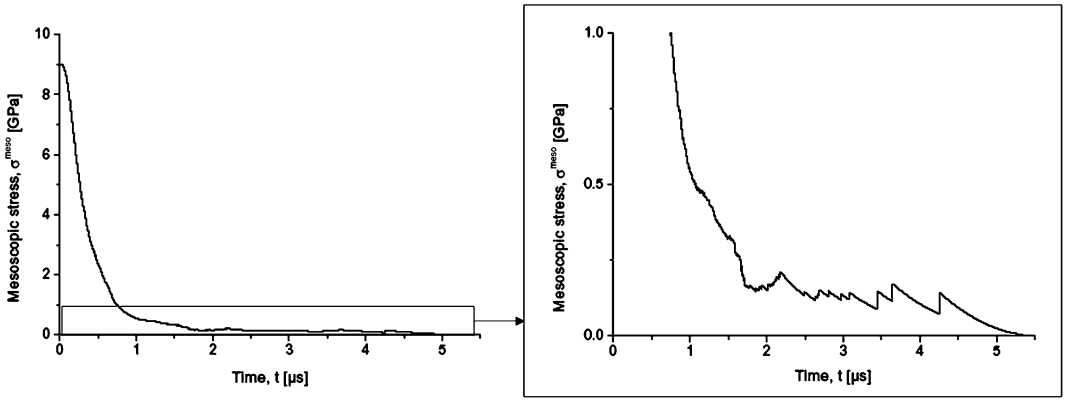

Fig. 13. Mesoscopic normal stress vs. time $\sigma^{\text{meso}}(t)$ obtained with the model applying the following constants: $V_{\text{f}} = 300$ m/s, $\chi = 1000$, $\delta = 5$ μm, $\Gamma_{\text{c}} = 0.45$, $V_{\text{b}} = 60$ m/s.

stantially shorter than the time obtained by the model ($t = 2.5$ μs). This difference can be explained by inaccuracies of measurement. Indeed, the analysis of the mean values ΔX_{i} and ΔY_{i} is rather complex. Nevertheless, the global criterion can be estimated if the values ΔX_{i} and ΔY_{i} are not optimal. The total time of spalling for one cell is: $t_{\text{total}} = t_a + t_{\max}$, Fig. 12,

$$\text{with } t_a = \frac{\overline{\Delta X_{\text{i}}} - a_{\text{moy}}}{\frac{3}{2} V_{\text{f}}},$$

$$\text{and } t_{\max} = \frac{\delta \Gamma_{\text{c}}}{V_{\text{b}}} + \frac{\Delta Y_{\text{i}}}{2 V_{\text{c}}}, \text{ Table 6.}$$

In present case, the loading time t_c must be longer or equal to t_{total}.

Thus, the following relation can be obtained:

$$t_c \geqslant t_{total}, \quad t_{total} = \frac{\Delta X_i - a_{moy}}{\frac{3}{2} V_F} + \frac{\Gamma_c \delta}{V_b} + \frac{\Delta Y_i}{2V_c}. \tag{17}$$

With $\delta = 5$ μm, Eq. (17) becomes a decreasing function of ΔX_i. When ΔX_i and ΔY_i are positive or zero, a range of ΔX_i and ΔY_i can be found in which the measured values are correct, this is shown in Fig. 14. This figure shows that some experimental points are apart from the validity range. These points must be rejected. This explains to some extend why the calculated total time of spalling is longer than the measured time. By elimination, those points one obtains, as it is shown in Fig. 15, the time evolution of the mesoscopic normal stress.

By application of the meso modelling shown in Fig. 15 and by using the definition of the mean time integral, the mean macroscopic stress of spalling predicted by the model can be determined

$$\overline{\sigma^{macro}} = \frac{1}{\Delta t} \int_{t_d}^{t_{spall}} \sigma^{meso}(t)\, dt, \tag{18}$$

where $\Delta t = t_{spall} - t_d$ is the time interval of integration. The longest interval is, of course, between the instants when the micro-crack starts to propagate, t_d, and it ends at the instant of the complete separation, when the normal stress is zero, t_{spall}. The curve shown in Fig. 15 was obtained with the hypothesis that all cells nucleate at the same time, thus $t_d = 0$.

The macroscopic spall stress calculated by the model for the target 5 is $\sigma^{macro} = 0.99$ GPa. This value is lower as compared with the experimental value obtained with the acoustic approximation. For target 5, the critical time for spalling is 1.9 μs. For this value of t_c, the respective value of σ^{macro} found from experiments is 4.91 GPa, Table 2. It can noticed that there is a substantial difference between these two results. Such difference can be explained by several hypotheses. The first one, the stress calculated by acoustic approach

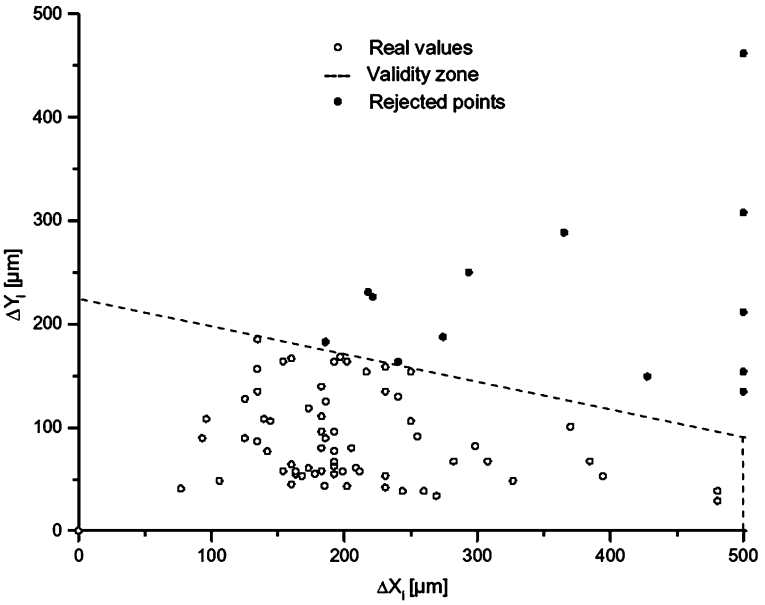

Fig. 14. Validity zone for ΔX_i and ΔY_i measurements.

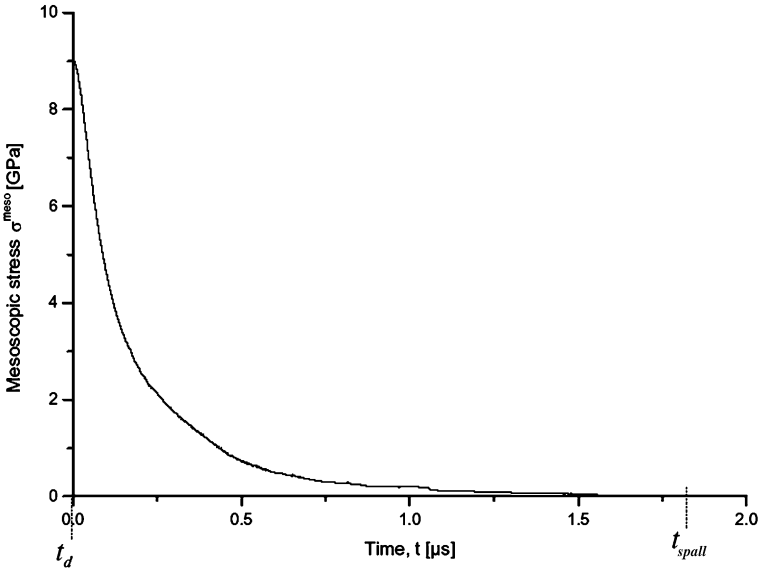

Fig. 15. Mesoscopic stress vs. total time $\sigma^{\text{meso}}(t)$ without eliminated values.

is overestimated because the hypothesis of perfectly rectangular load was applied. Next, the hypothesis of nucleation time is incorrect. It is assumed till now that cells nucleate at the same time, $t_{\text{d}} = 0$.

Thereafter, it was decided to analyse the nucleation time. It is probable that there is a relation between the nucleation time and the size of hard particles, thus $t_{\text{d}}(\Delta X_{\text{i}})$. The larger ΔX_{i} nucleate earlier. Different evolution laws of nucleation time were analyzed, the result is plotted in Fig. 16. With the rational evolution of nucleation time in function of ΔX_{i}, it is interesting to note that the macroscopic stress increases to value 2.84 GPa. Values of the material constants used in this version of the model are given in Table 7. It can

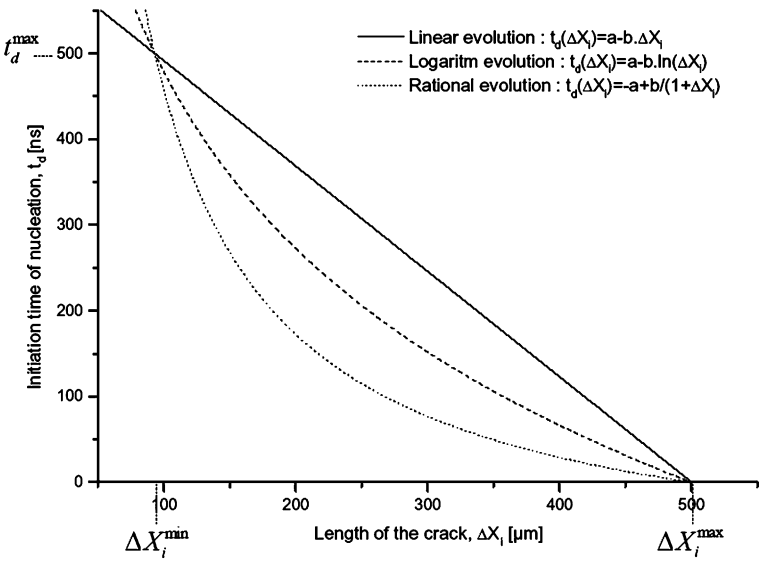

Fig. 16. Relation between the initiation time of nucleation and the length of the crack ΔX_{i}.

Table 7
Summary of constants values used in the model

γ_e [j/m^2]	χ	a_{moy} [μm]	V_f [m/s]	δ [μm]	Γ_c	V_b [m/s]	V_c [m/s]	t_d^{max} [ns]
1	1000	5	200	5	0.45	60	65	800

noticed that the macroscopic stress calculated by the model is always lower as compared with the value obtained with the acoustic approximation. This difference can be explained by the fact that there are too many parameters to identify: 23 constants on the whole. That is why, for a future study, a numerical approach via the finite element calculations will be implemented to reduce parameters number to identify. But the mean reason may be a substantial underestimation of the flow stress τ_0. The value of τ_0 was assumed after experimental data shown in Fig. 9 at $\dot{\Gamma} \sim 10^5$ s^{-1} whereas the local shear strain rate in the core of the adiabatic shear band can read the level of $\sim 10^7$ s^{-1}. At this strain rate the flow stress is much higher. Lack of experimental data for Ti alloys and for such range of strain rate limits a more exact application of the model.

6. Conclusions

The main purpose of this study was to examine physical mechanisms of spall fracture for Ti–6Al–4V alloy on the incipient level, to identify the main stages of spalling in the meso-scale, and to apply the meso-macro model to this alloy. An automated high performance gas launcher has been developed in the LPMM-Metz for precisely controlled plate impact tests. The series of eleven tests at different impact velocities have been performed leading to different loading times, and the level of the normal stress for the incipient spall in function of the incident pulse duration has been determined. Such analysis has yielded a preliminary data in the form of the critical stress of spalling vs. the pulse duration. Those data permitted to determine material constants for the cumulative failure criterion.

Complete microscopic observations (SEM and optical) have been performed with cross-sections of the targets. The microscopic study was performed to understand better the effect of microstructure on the physical mechanisms of nucleation, growth and coalescence of micro-cracks and micro-voids. It has been confirmed that the orientation of microstructure has a direct influence, due to two microstructural α and β-phases, on failure mechanisms by means of distribution of nucleation sites and decohesion between the harder particles (α-phase) and the softer lattice (β-phase). The interesting point in Ti–6Al–4V alloy is the development of micro-voids. A significant amount of very small micro-voids in the region of the expected spall plane was observed. Two mechanisms of the initial stages of failure were found, that is the micro-voids formation which is different whether the lamellae are parallel to the plane wave or whether they are inclined to an angle. Further studies on micromechanics of failure at different stages of the material separation would be important in order to obtain a complete picture of spalling in Ti–6Al–4V alloy.

Some results of measurements have lead to formulation of a model of spalling which accounts quasi-brittle fracture and ductile shear banding. The model is based on the numerous post-mortem microscopic observations of spall specimens and mesoscale approximations. This approach allows to determine the macroscopic stress of spalling in function of loading time and damage level for a very particular Ti material. In a perspective, an improved version of the model could be applied in any other hard materials, like armor steels where a dimple models are not valid. The preliminary obtained results are in good agreement with physical mechanisms which occur during spall fracture, even if the value calculated by the model is still lower as compared with the value found from experiments. The disagreement is due to lack of experimental data needed to precisely determine 23 material constants. In the future an attempt could be pursued to verify the model proposed by experiments of fracture dynamics.

In perspective, the first stage of failure in the meso-model of spalling discussed in this paper: namely nucleation of micro-voids will be analysed. A numerical approach will allow to calculate the local stress

during the micro-voids nucleation which will then be implemented in the meso-model of spalling. It is assumed that the obtained results will permit to explain the void nucleation observed experimentally and to calculate the evolution of the local stresses of micro-voids nucleation.

Acknowledgements

The research reported herein has been sponsored in part by the US Army through its European Research Office, Contract N62558-02-M-5857.

Acknowledgements for financial support are also due to the French Ministry of Education (XB) and CNRS-France (JRK).

References

Arrieta, H.V., Espinosa, H.D., 2001. The role of thermal activation on dynamic stress-induced inelasticity and damage in Ti–6Al–4V. Mechanics of Materials 33, 573–591.

Boidin, X., Chevrier, P., Klepaczko, J.R., 2003. Validation of a fracture model based on mesoscale approach for spalling of hard steel and aluminium alloy. Journal de Physique IV 110, 550–845.

Cagnoux, J., 1985. Déformation et ruine d'un verre pyrex soumis à un choc intense: étude expérimentale et modélisation du comportement. Ph.D. Thesis of Poitiers University.

Chevrier, P., Klepaczko, J.R., 1997. Discussion of fracture criteria in spall mechanics. Engineering Transaction 45, 47–70.

Chevrier, P., Klepaczko, J.R., 1999. Spall fracture: mechanical and microstructural aspects. Engineering Fracture Mechanics 63, 273–294.

Curran, D.R., Seaman, L., Shockey, D.A., 1987. Dynamic failure of solidsPhysics Reports 147, vol. 5. North-Holland, Amsterdam, pp. 253–388.

Dremin, A.N., Molodets, A.M., 1985. On the spall strength of metals. In: Proceedings of the International Symposium on Intense Dynamic Loading and its Effects. Beijing: Pergamon Press, p. 13.

Follansbee, P.S., Gray, I.G.T., 1989. An analysis of the low temperature, low- and high-strain rate deformation of Ti–6Al–4V. Metallurgical Transactions 20A, 863–874.

Gilman, J.J., 1960. Direct measurements of surface energies of crystals. Journal of Applied Physics 31, 2208–2218.

Grady, D.E., 1988. The spall strength of condensed matter. Journal of the Mechanics and Physics of Solids 36 (3), 353–384.

Hanim, S., Klepaczko, J.R., 1999. Numerical study of spalling in an aluminium alloy 7020-T6. International Journal of Impact Engineering 22, 649–673.

Klepaczko, J.R., 1988. A general approach to rate sensitivity and constitutive modelling of BCC metals. In: Effects of fast transient loadings. Rotterdam, pp. 3–35.

Klepaczko, J.R., 1990. Dynamic crack initiation, some experimental methods and modelling. In: Klepaczko, J.R. (Ed.), Crack Dynamics in Metallic Materials. Springer-Verlag, Vienna, New York, pp. 428–445.

Klepaczko, J.R., Chevrier, P., 2003. A meso-model of spalling with thermal coupling for hard metallic materials. Engineering Fracture Mechanics 70, 2543–2558.

Marchand, A., Duffy, J., 1988. An experimental study of the formation process of adiabatic shear bands in a structural steel. Journal of the Mechanics and Physics of Solids 36 (3), 251–283.

Me-Bar, Y., Boas, M., Rosenberg, Z., 1987. Spall studies on Ti–6Al–4V. Materials Science and Engineering 85, 77–84.

Mescheryakov, Yu.I., Divakov, A.K., Zhigacheva, N.I., Petrov, Yu.A., 1999. Spall strength and phase transformation in titanium alloys in impact loading. The Physics of Metals and Metallography 87 (5), 443–449.

Orowan, E., 1948. Fracture and strength of solids. Reports on Progress in Physics 12, 185–232.

Seo, S., Min, O., Yang, H., 2005. Constitutive equation for Ti–6Al–4V at high temperature measured using the SHPB technique. International Journal of Impact Engineering 31, 735–754.

Tuler, F.R., Butcher, B.M., 1968. A criterion for the time dependence of dynamic fracture. International Journal of Fracture 26 (4), 322–328.

Wright, T.W., Ockendon, H., 1992. A model for fully formed shear bands. Journal of the Mechanics and Physics of Solids 40 (6), 1217–1226.

Wulf, G.L., 1979. High-strain rate compression of titanium and some titanium alloys. International Journal of Mechanical Sciences 21, 713–718.

Zhurkov, S.N., 1965. Kinetic concept of the strength of solids. International Journal of Fracture 1, 311–323.